Global seafloor topography from a least-squares inversion of altimetry-based high-resolution mean sea surface and shipboard soundings

Stéphane Calmant,[1,2] Muriel Berge-Nguyen[2] and Anny Cazenave[2]

[1]*Laboratoire de Geophysique, IRD, BP A5*, *Noumea, Nouvelle Caledonie*
[2]*LEGOS,* 18 *av. E. Belin,* 31400 *Toulouse, France. E-mail: calmant@notos.cst.cnes.fr*

SUMMARY

We present a new worldwide $1/16° \times 1/16°$ map of seafloor topography computed from an iterative inversion combining altimetry measurements of the marine geoid and shipboard echo soundings from the global National Geophysical Data Center (NGDC) database. The input geoid data for this computation are derived from altimetry measurements of the sea-surface height from the ERS-1 Geodetic Mission, and the GEOSAT, ERS-1 and Topex-Poseidon Exact Repeat Missions. To calculate the seafloor topography from sea surface height measurements, it is necessary to take the regional isostatic compensation of the topographic load into account. For that purpose, we consider a model of elastic flexure of the oceanic lithosphere in which the elastic plate thickness increases with crustal age. With the solution, we provide an uncertainty map that reflects the uneven distribution of and errors in the data, and uncertainties in the model parameters, as well as the increase of the geopotential error with the deepening of the seafloor. The bathymetric solution is compared with the Smith & Sandwell's (1997, *Science,* **227,** 1956–1962) solution. The root mean square difference between the two amounts to 350 m. However the two maps agree within 150 m over 65 per cent of the ocean surface.

Key words: geoid anomalies, oceanic lithosphere, topography.

1 INTRODUCTION

Because the oceans cover roughly 70 per cent of the Earth' surface, knowledge of seafloor topography is important for numerous scientific investigations, for example in marine geophysics, physical oceanography and marine biology. It is also important for exploration of living and mineral resources. However, although some specific areas such as the Economic Zones of North American and European countries have been almost fully covered by multibeam echo-sounders, most of the oceans, especially in the Southern Hemisphere, remain uncharted. Direct mapping of topography from space is feasible only over continental areas. This has recently been achieved by the US-Shuttle Radar Topography Mission, which has provided 3-D topography of the continents with an unprecedented vertical precision of ~10 m. By contrast, seafloor topography is not directly accessible to remote sensing by radar because electromagnetic waves do not penetrate into water. Furthermore, it would take several tens of years to map the entire ocean floor using conventional shipboard measurements, not to mention the prohibitive cost. Fortunately, satellite altimetry offers an indirect way to measure seafloor topography from space. Satellite altimetry measures the mean sea surface, the undulations of which reflect, at least at short wavelengths, the topography of the seafloor and its isostatic compensation. If the latter effect can be modelled with sufficient

precision, altimetry-derived undulations of the mean sea surface, which approximate the marine geoid, can be used to derive bathymetric maps over the entire oceanic domain. About two decades ago, bathymetric prediction was largely concerned with detecting uncharted seamounts from their gravitational signature (for example, Lambeck & Coleman 1982; Cazenave & Dominh 1984; Freedman & Parsons 1986, among others). Filters have also been designed to model seamount height and location along satellite tracks (Sailor 1982; Lazarewicz & Schwank 1982; White *et al.* 1983). The first global bathymetric maps based on satellite altimetry were published by Dixon & Parke (1983) and Sandwell (1984). Inversion of altimetry data to compute the bathymetry was initially performed along individual satellite tracks (that is, in 1-D) using the admittance method (Dixon *et al.* 1983; Vogt & Jung 1991; Jung & Vogt 1992; Goodwillie & Watts 1993). In addition, Baudry *et al.* (1987) and Craig & Sandwell (1988) performed 1-D adjustment of synthetic profiles along satellite tracks. The advent of dense altimetric coverage of the oceans by the GEOSAT (1985–1986) and ERS-1 (1994–1995) Geodetic Missions (GM) increased the horizontal resolution to better than 10 km everywhere. These dense data sets (either used alone or merged with echo soundings when available) have been used to compute 2-D estimates of bathymetry (Baudry & Calmant 1991, 1996; Smith & Sandwell 1994, 1997; Sichoix & Bonneville 1996; Ramillien & Cazenave 1997; Ramillien & Wright 2000). Sandwell

& Smith (2000) recently reviewed the computation of seafloor topography from altimetry and echo sounding data.

Most studies have been conducted in the Fourier domain where convolution operations are replaced by spectral products. In addition, reduction to the first term of the infinite power series of the bathymetry to gravity ratio, as proposed by Parker (1973), has often been used. However, as discussed by Ribe (1982), this truncation severely underestimates the gravity to bathymetry ratio at wavelengths shorter than 50 km (see also Calmant & Baudry 1996) and with it, the amplitude of the bathymetry. Moreover, the gravity signature of the predicted bathymetry computed using Parker's fully developed series does not reproduce the gravity data from which that bathymetry was derived. Nevertheless, higher-order terms can be accounted for by an iterative process (Baudry & Calmant 1991, 1996).

In studies conducted in the Fourier domain, it is not possible to combine gravity/geoid data with sparse *in situ* bathymetry data in a single calculation. The two data sets must be processed separately. Instead of being included in the inversion, the shipborne data are used to constrain the gravity-derived bathymetric prediction (Smith & Sandwell 1994, 1997; Baudry & Calmant 1996; Sichoix & Bonneville 1996). In addition, the data have to be interpolated onto regular grids to take full advantage of Fast Fourier Transform techniques. In spectral methods, investigators invert the spectra of the gridded gravity data directly without dealing with noise in the data. Thus the predicted bathymetry potentially includes the spectrum of the noise. Moreover these methods require a stabilization procedure (Baudry & Calmant 1991, 1996; Ramillien & Cazenave 1997) or tuned filters (Smith & Sandwell 1994, 1997; Sichoix & Bonneville 1996) to avoid or minimize the development of unrealistic short-wavelength undulations.

Prediction of the bathymetry at short and intermediate wavelengths (≤ 500 km) from its gravity signature must account for compensation of the load of the submarine topography within the underlying oceanic lithosphere (Dixon *et al.* 1983). Watts (1978) established that the dominant mode of compensation of seamounts results from the elastic flexure of the oceanic lithosphere. Computation of this regional compensation mechanism requires that the age of both lithosphere and topographic load be known. Unfortunately, the latter is unknown for most of the world's seamounts. Ramillien & Cazenave (1997) and Ramillien & Wright (2000) applied the empirical relationship derived by Watts (1978) to model spatial variations of compensation using only the age of the plate. Baudry & Calmant (1996), and Sichoix & Bonneville (1996) determined the compensation modes in their study area from previous works in the vicinity of the study area and generalized their pointwise results to the entire domain over which the prediction was performed. Smith & Sandwell (1994, 1997) used separate procedures to characterise the isostatic compensation at short (less than 160 km) and intermediate (between 160 and 800 km) wavelengths. They bandpassed the gravity data in order to remove signal in the 160–800 km waveband and deliberately did not predict bathymetry in this waveband. At short wavelengths (less than 160 km), they downward continued their filtered gravity data and used an inverse Nettleton procedure to derive local values of the bathymetry to gravity ratio (equivalent to an inverse Bouguer correction). This method is applicable where echo soundings are available and relevant of the feature the topography of which is predicted. A transfer function was then defined throughout the whole oceanic domain through interpolation onto a regular grid and finally multiplied by the downward-continued gravity signature to derive the short-wavelength component of the bathymetry.

In the present study, we perform a global computation of seafloor topography, applying generalized least-squares theory. The solution (of which the formalism was originally developed by Calmant 1994), is derived in the spatial domain through a linear combination of altimetry products (mean sea surface height and/or marine gravity anomaly) and shipboard measurements (depth and/or gravity anomaly profiles). This approach avoids some of the drawbacks of spectral methods. The most noticeable improvement is the possibility of combining sparse observations from different sources. Based on a least-squares fit, the method predicts a bathymetry solution in which values and corresponding uncertainties are consistent with the uncertainties of each data set and model simplifications, if any. It also accounts for the intrinsic non-linearity between gravity (either in the form of gravity anomalies or geoid undulations) and seafloor topography. The map of seafloor topography around New Zealand recently computed by Ramillien & Wright (2000) is based on this approach.

2 DATA ANALYSIS

2.1 Altimetry products

Satellite altimetry measures the instantaneous sea surface height relative to a reference ellipsoid. When corrected for radar propagation errors (through the ionosphere and troposphere), sea state bias, inverted barometer response, and solid Earth, ocean and polar tides, such measurements provide an estimate of the mean sea surface, which, to first order, coincides with the geoid (an equipotential surface of the Earth's gravity field). Instantaneous sea surface heights at a given location differ from the mean of such heights due to the presence of transient oceanographic signals. For geophysical investigations, it is critical to remove the transient oceanic effects. Recently, Hernandez & Schaeffer (2000) computed a mean sea-surface solution based on an optimal inverse method and corrected for mesoscale ocean variability. Dense altimetry data from the ERS-1 GM, complemented by data from the Exact Repeat Missions (ERM) of Topex/Poseidon (T/P), ERS-1 and GEOSAT, were used for the computation. First, mean along-track sea surface profiles were computed for the entire ERM of the three satellites. Then, sea surface anomalies and associated spatial and temporal covariance functions were determined from these mean profiles. To improve resolution, data from the ERS-1 GM were incorporated and the total data set was inverted through a least-squares fit onto a regular $1/16° \times 1/16°$ grid following the method developed by Mazzega & Houry (1989). In particular, the empirical covariance functions accounting for the oceanographic transient perturbations were incorporated into the covariance matrices constructed for the inversion of the altimetry data. In this way, the ERS-1 GM data were also corrected for the time-varying ocean contribution, as deduced from the T/P data. Conversely, the GEOSAT GM data were not included because no exact repeat mission took place over the same period, so the computation of covariance functions were not possible. The corresponding mean sea surface map and associated uncertainty map (also with a $1/16° \times 1/16°$ grid step) were used as input to our present bathymetry computation. The mean sea surface map and computational procedures are available on the web site: www.cls.fr/mss.

2.2 Shipboard soundings

We used the database of shipboard echo soundings collected by the US National Geophysical Data Centre (NGDC), available on

the Geodas Trackline Geophysics CDROM, version 4.0 (Sharman 1998). The quality of these shipboard soundings is highly variable (Smith 1993). In the period up to the 1980s, when ship positioning by satellites used the TRANSIT system, errors in ship positions could reach 1 km (Nishimura & Forsyth 1988), as is particularly visible at crossover points. Since the late 1980s, the Global Positioning System (GPS) system provides 100 m precision in ship positioning. However less than 10 per cent of the NGDC data were collected during GPS-navigated cruises (Smith 1993). More dramatically, hand digitisation of sounding profiles performed for incorporation in global databases had led to long-wavelength errors of several hundreds of meters (Smith 1993). Tests performed during the present analysis have shown that because of this heterogeneity, shipboard sounding data should not be considered as a primary data set for computing bathymetry when combined with altimetry products. Rather, echo soundings and altimetry products should be considered as complementary data with their own uncertainties. Fig. 1 shows the geographical distribution of the shipboard data used in this study.

3 METHOD

The topography of the ocean floor is the result of four main physical processes: (1) oceanic plate formation at mid-oceanic ridges and consumption at subduction zones, (2) intraplate volcanism, (3) cooling and contraction of oceanic plates, and (4) deformation of the lithosphere under topographic loads. Thermal contraction of the oceanic lithosphere leads to long-wavelength subsidence of the seafloor away from mid-ocean ridges and short-wavelength topographic steps across transform faults and fracture zones. Topographic loading has two principal effects on the seafloor: short-wavelength elastic flexure of the lithosphere, in response to local loads, and long-wavelength bulge at trenches, where the subducting oceanic lithosphere is loaded by the overriding plate. Intraplate volcanism produces short- and intermediate-wavelength features on the seafloor. Active as well as fossil tectonic processes generate numerous other short and medium wavelength features. The long-wavelength component of the topography cannot reasonably be modelled using altimetry-derived geoid data because at long-wavelengths, the geoid also reflects deep mantle processes. However the long-wavelength topographic component can be estimated using low-resolution bathymetric grids based on shipboard profiles. In contrast, dense satellite altimetry data are particularly suitable for determining short-wavelength topographic features poorly charted by ships.

3.1 Generalized least-squares inversion

The approach used in this study to recover the short-wavelength seafloor topography is that developed by Calmant (1994) and employs a discrete inverse theory (Menke 1989; Tarantola 1987). The bathymetric depths are computed as the least-squares solution of model parameters in a discrete inverse problem. The model parameters obtained from the inversion consist of discrete estimates of bathymetric depth regularly spaced on a grid and the solution is constructed as a linear combination of the data with optimal coefficients in the least-squares sense. The coefficients are determined through an iterative process from the physical relationship between each datum and each model parameter. *A priori* information on the model parameters and a description of the errors that affect data and model are taken into account (Tarantola 1987). The modelled seafloor depth $\mathbf{b}_n(r)$ at location r, which corresponds to the *a*

posteriori value of the model parameters at the *n*th iteration, is given by:

$$\mathbf{b}_n(r) = \mathbf{b}_o(r) + \mathbf{C}_{rr'}\mathbf{G}_n^T \left[\mathbf{G}_n\mathbf{C}_{rr'}\mathbf{G}_n^T + \mathbf{E}_{ss'}\right]^{-1} [d(s) - g(s) + \mathbf{G}_n [\mathbf{b}_{n-1}(r) - \mathbf{b}_o(r)]] \quad (1)$$

where r and s are the location of estimate and data, respectively, $\mathbf{b}_o(r)$ is a vector containing the *a priori* values of the model parameters, $\mathbf{b}_{n-1}(r)$ is a vector containing the a *a posteriori* value of the model parameters at the $(n-1)$ iteration, $\mathbf{G}_n$, and its transpose $\mathbf{G}_n^T$, are the iteratively improved model matrices whose elements are constructed by a first-order development of the direct, non-linear relationship $g(r, s)$ between the data $\mathbf{d}(s)$ and model parameters. The covariance matrix $\mathbf{C}_{rr'}$ accounts for uncertainties of the *a priori* solution and the matrix $\mathbf{E}_{ss'}$ accounts for data and model uncertainties. The main advantage of this method is that the data sets used to construct the bathymetric map can be of different kinds. In this study, the data set consists of an altimetry-derived geoid grid and shipboard bathymetric profiles. It is worth noting that the data need not be aligned in a regular grid as is the case for spectral methods. The model parameters stand for different geophysical quantities according to the data type. As far as echo soundings are concerned, the bathymetry modelled on each gridpoint represents a discrete averaged value of the actual bathymetry over the cell centred on that gridpoint. We have computed the median value of all soundings in each calculation grid cell. For such grid points, the model parameters equal these normal data points. For geoid undulations, the relationship between data and model parameters is based on the gravitational perturbation generated by the mass anomaly associated with the seafloor relief. The geoid undulation is not linearly related to the height of the mass anomaly. Indeed, in eq. (1) above, g is not a linear function of $\mathbf{b}(r)$ and its derivatives with respect to $\mathbf{b}(r)$ are not independent of $\mathbf{b}(r)$. So the coefficients of the $\mathbf{G}$ matrix, determined using derivatives of g with respect to $\mathbf{b}(r)$, are approximated when computed with $\mathbf{b}_o(r)$. For this reason, the final values of the model parameters $\mathbf{b}(r)$ are obtained through an iterative process using improved estimates of the derivatives of g as $\mathbf{b}(r)$ converges towards its final value. The linearized expressions for g and its derivatives used to compute the coefficients of the $\mathbf{G}$ matrix are given in Calmant (1994).

3.2 Isostatic compensation

The seafloor topography is not the only density contrast that gives rise to geoid anomalies. Undulations of density interfaces within the oceanic lithosphere, such as the Moho discontinuity, also produce lateral density contrasts, hence geoid anomalies. The undulations of the lithospheric density contrasts are mostly due to compensation of the bathymetric features that load the lithosphere. In this study, both local (Airy type) and regional compensation models have been considered. In the context of regional compensation, the shape of the lithospheric internal density contrast is modelled through the flexural response of a thin elastic plate due to surface load (Watts *et al.* 1975). The plate deflection is controlled by the flexural parameter α, related to the plate stiffness D and equivalent elastic thickness T_e by:

$$\alpha = \sqrt[4]{\frac{4D}{\gamma\,\Delta\rho'}}, \quad D = T_e^3 \frac{E}{12(1 - \nu^2)} \quad (2)$$

where E and ν are the Young's modulus and Poisson's ratio. $\Delta\rho$ is the density contrast of the load relative to surrounding sea water. $\Delta\rho'$ is the density contrast across the deflected density interface
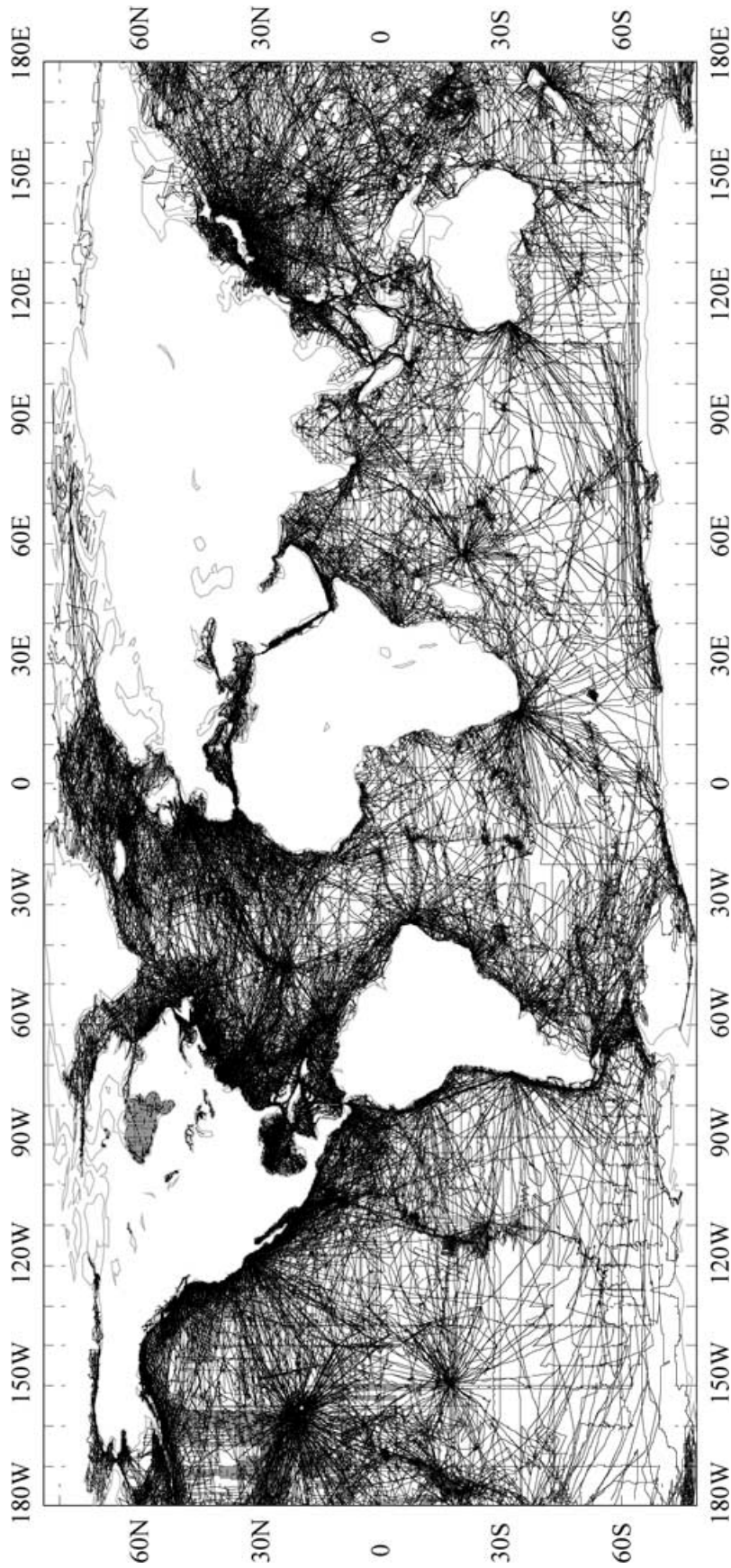
Figure 1. Geographical distribution of the NGDC *in situ* bathymetric profiles used in this study.

(Moho). This regional compensation model has been widely used to study the mechanical behaviour of the oceanic lithosphere loaded by intraplate volcanoes (for instance, McNutt & Menard 1978; Watts 1978; Calmant *et al.* 1990; Goodwillie & Watts 1993, among many others). The Airy model of local compensation is the limiting case when T_e and α tend towards zero.

The geoid step at fracture zones may be derived from the bathymetric step through cooling plate models (for instance, GDH1, Stein & Stein 1992). However, no specific algorithm has been developed here to invert the geoid step into bathymetric step since the signature due to plate age difference is often merged with that of other bathymetric features (for example, volcanic ridges or trenches) which border such faults. In this study, the gravity signature of transform faults has been processed as if it were the signature of volcanoes.

3.3 *A posteriori* uncertainties

Least-squares adjustment allows data and model uncertainties to be taken into account in the computation. As a consequence, an uncertainty associated with each computed bathymetric value can be computed. This provides insight into the quality of the solution and provides more information than global statistics. The uncertainties associated with the *a posteriori* model parameters are given by the diagonal elements of the *a posteriori* covariance matrix $\Sigma_{rr'}$,:

$$\sigma(r) = \sqrt{\Sigma_{rr'}(r = r')} \qquad (3)$$

where $\Sigma_{rr'}$, can be approximated, for iterative schemes, by (Tarantola 1987):

$$\Sigma_{rr'} = \mathbf{C}_{rr'} - \mathbf{C}_{rr'}\mathbf{G}_N^T \left[\mathbf{G}_N\mathbf{C}_{rr'}\mathbf{G}_N^T + \mathbf{E}_{ss'}\right]^{-1}\mathbf{G}_N\mathbf{C}_{rr'} \qquad (4)$$

where N represents the index of final iteration to reach convergence. In eqs (3) and (4), *a posteriori* uncertainties are independent of the actual data values. They reflect how input uncertainties are propagated through the modelling process. They neither reflect how well the *a posteriori* model parameters fit the data nor any possible mismodelling of data uncertainty. This is due to the computation scheme adopted in this study that is based on data inversion on narrow grid cells. In addition, *a posteriori* uncertainties do not reflect model errors, since the latter are not taken into account. These model errors are related to the long-wavelength part of the solution to which the prediction is added, as well as to uncertainties in the compensation model and density values (Baudry & Calmant 1996). Disregarding these model errors leads to underestimation of the *a posteriori* uncertainties. However, accounting for these model errors rigorously appears to be extremely expensive in terms of computer time and we decided not to include them in the present computation. Nevertheless, in order to derive more realistic uncertainties, we used the unit covariance factor to scale the formal *a posteriori* covariance associated with the solution globally. The unit covariance factor χ^2 measures the ratio of the misfit to the data uncertainties σ_d. We determined an approximate value of this unit covariance factor by computing the misfit to the echo sounding data only:

$$\chi^2 = \frac{1}{M} \sum \frac{[d(s) - b(s)]^2}{\sigma_d(s)^2} \qquad (5)$$

where M is the number of pixels where echo soundings $d(s)$ exist and s their position on the grid. In eq. (5), $d(s)$ does not represent the actual echo soundings but the median value of all soundings lying in each grid cell. Finally, uncertainties $\bar{\sigma}(r)$ that also account for the misfit are obtained by scaling the formal *a posteriori* variances $\sigma^2(r)$ with the unit covariance factor such that:

$$\bar{\sigma}^2(r) = \chi^2\sigma^2(r). \qquad (6)$$

We would not expect discrepancies between predicted bathymetry and echo sounding data to be randomly distributed. For example, errors related to incorrect T_e values are more likely to be found in old oceanic basins than in the vicinity of mid oceanic ridges. Because χ^2 is a mean value over the whole oceanic domain, it is likely that uncertainties are underestimated in rough areas of old seafloor (old seamounts for which T_e is actually low whereas a large value was used in the computation). On the other hand, uncertainties may be overestimated in smooth areas such as basins devoid of seamounts, where T_e does not matter. Nevertheless, production of an uncertainty map is a step forward compared to previous studies.

4 NUMERICAL COMPUTATIONS

The method implies the use of an *a priori* solution. As for all inversions of potential fields, this *a priori* solution is important since the data-inversion process mostly acts to construct high-order corrections to the *a priori* solution. We have produced the *a priori* solution for the seafloor topography by computing the difference between a long-wavelength reference depth map and a high-resolution bathymetric map. The long-wavelength reference is derived from the ETOPO-5 bathymetric grid (National Geophysical Data Center 1988) in which wavelengths shorter than 2000 km have been filtered out. For the high-resolution map, we tested several solutions (Ramillien & Cazenave 1997, ETOPO-5; Smith & Sandwell (1997)). We finally retained that of Smith & Sandwell (1997). Indeed, in our calculation, this map led to fewer iterations before reaching convergence. It must be pointed out that with this procedure, the predicted bathymetry is not associated solely with the high-resolution map selected to start the iteration process, but also with the long-wavelength reference map.

We modelled the uncertainty associated with the *a priori* solution through the following empirical function:

$$\mathbf{C}_{rr'} = \frac{\sigma_o^2}{1 + \frac{l^2}{\lambda_c^2}} \qquad (7)$$

where l is the distance between grid points at r and r'. The cut-off wavelength λ_c has been empirically set at 20 km. We assigned a 500-m uncertainty σ_o to the *a priori* solution. This value is larger than the rms errors quoted by Smith & Sandwell (1997) for their high-resolution map. However, this σ_o value includes the uncertainty in the long-wavelength reference and enables the *a priori* solution to constrain the final solution weakly.

Concerning the isostatic compensation, the model function $g(r, s)$ relating the geoid data to the model parameters requires that the flexural rigidity of the plate be known everywhere. The deflection of the seafloor under a volcanic load depends on the elastic plate thickness at the time of loading. Elastic plate thickness increases with the depth of an isotherm in the range $350°$C–$450°$C (Watts *et al.* 1980; Watts & Ribe 1984; Calmant & Cazenave 1987; Calmant *et al.* 1990). While crustal age is rather well known, the age of the loads, hence the times of loading, are far globally known. Times of loading have been measured at a few specific locations where the bathymetry is already well known. Elsewhere, times of loading have to be guessed, between zero and the age of plate itself. For the present study, we assumed that the times of loading are everywhere the age of the plate itself, or in other words, that all bathymetric features are recent. This assumption will have little consequence on the predicted bathymetry for off-ridge seamounts

(edifices that are young with respect to the age of plate), for structures such as elastic bulge and trenches that are not compensated and for fracture zones which compensation is not accommodated by the deflection of density interfaces within the upper lithosphere. In contrast, this assumption will lead to underestimation of the height of old on-ridge seamounts (features of approximately the same age as the plate), elongated ridges and massive plateaus. Indeed, assuming zero loading age underestimates the negative contribution of the compensating mass to the total geoid undulation. This assumption tends to deteriorate the bathymetric solution at places where the elastic thickness is known and is noticeably different from the assumed value. However, these areas are very sparse and have already been covered by oceanographic cruises, in particular concerning the large ridges and plateaus. As a result, the error caused by assigning an incorrect value of T_e is damped by the availability of dense *in situ* bathymetric data that, unlike altimetry-derived data, are not affected by any assumption on T_e. In uncharted areas, the older the plate, the older the unknown seamounts may be, leading to larger errors with respect to the actual T_e value. However, Baudry & Calmant (1991) showed that for the S6 seamount, located south of the Cook-Austral chain in the south central Pacific, the maximum error on the bathymetric height due to extreme error on T_e is only ∼300 m.

Complete modelling would imply that all parameters, such as elastic thickness and densities involved in the computation of the deflection, are included in the list of the unknown model parameters. However, Ramillien & Mazzega (1999) showed that including these parameters makes the inversion numerically unstable. Tests showed that the parameter values change little while iterating and the final values remain close to the *a priori* values. Because such a full modelling is also computer-time consuming, we decided not to solve for the elastic thicknesses and densities.

We considered the crustal age map derived by Muller *et al.* (1997). We assumed that the elastic thickness T_e follows the intermediate 400°**C** isotherm (Calmant & Cazenave 1987), leading to the following empirical relationship (T_e in km and age in Ma):

$$T_e = 2.7 x age^{0.5} \tag{8}$$

The map of Muller *et al.* (1997) includes large gaps. In areas located close to continental margins, where the seafloor is old, we have assigned an age of a 200 Ma. Our computation procedure dictates that, at the border of continents, we focus on small features that are superimpose on longer wavelength structures and are mostly uncompensated. This minimizes the amplitude of the computed topography and avoids the numerical instabilities that develop in shallow areas such as the continental shelves. The only place where this procedure is clearly inadequate is in the belt of young backarc basins between the Australia and Pacific plates where no crustal age is available. In these areas, the depth of bathymetry may be underestimated.

Numerical computations were conducted on $0.5° \times 0.5°$ cells. While inversion is performed at each $1/16°$ grid cell, only the bathymetry solution at the central pixel is retained after inversion. Although computationally expensive, this procedure allows an overlap of 89 per cent between adjacent cells, avoiding edge effects. The main limitation of this scheme is the reduced size of the computation cells with respect to the typical waveband of the flexural compensation. The computed deflection (hence predicted bathymetry) will be underestimated if a large load lies outside the computation cell, but close enough for the deflection inside the cell be a significant amount of the maximum deflection produced under that load and last, if the elastic thickness is small enough for the overall deflection be significant.

Table 1. Values of general constants and lithospheric parameters used in the computation.

Parameter/constant	Numerical value
Lithospheric parameters	
Crustal thickness	6 km
Load density	2700 kg m^{-3}
Density of oceanic crust	2700 kg m^{-3}
Mantle density	3350 kg m^{-3}
General constants	
Mean gravity at Earth surface	9.81 m s^{-2}
Young's modulus	10^{12} SI
Poisson's ratio	0.25

nificant. In practice, the summit of the volcanoes is barely affected by the reduced size of the computation cells whereas the height of the edifice might be underestimated far from its center. In particular, the flexural moats flanking the large volcanoes such as these of the Hawaiian chain might be underestimated where not constrained by *in situ* data. It is worth noting that this drawback is shared with most studies whether conducted in the spectral or spatial domain although spectral methods enable that larger areas are processed using Fast Fourier Transforms. Because Ramillien & Wright (2000) performed a computation on a regional study, they could use larger cells ($2° \times 2°$) than in the present study, but nevertheless retained the inner 40 per cent of the cell, with an overlap between successive cells of only 36 per cent. Estimate of the computer time needed for a global inversion with $2° \times 2°$ cells led to prohibitive cost, incompatible with our current resources. Our choice of $0.5° \times 0.5°$ cells results thus from a compromise between computational resources and computational precision. To minimize the drawback mentioned above, we constrained the solution obtained in the inversion with ship sounding data (see next section). Note that the error introduced by using small cells is only significant around large seamounts, say 200–400 km wide, emplaced on young lithosphere, say 0–20 Ma old, which are otherwise well covered by *in situ* data for most of them. It is worth noting also that on the other hand, not to account for the compensation of loads outside the cell is a benefit when the relief at the outer rim of the cell is not compensated, like the ridges bordering the fracture zones.

When geoid data are used, the modelled depths correspond to the height of the mass anomaly above a reference regional level. Accordingly, the geoid undulations used in the inversion should reflect only shallow density contrasts. Wavelengths greater than 500 km have been filtered out of the mean sea surface for in order to remove the gravity signature of deep processes. We tested other cut-off values (from 150 km to 2000 km). But, the choice of a 500-km cut-off appears most compatible with the size of the computation cells and the wavelength of the signal contained in the *a priori* solution.

A height uncertainty of 3 cm has been assumed for the gridded geoid values. This corresponds to an upper bound of the uncertainty map published by Hernandez & Schaeffer (2000). Lower values can be found in their uncertainty map, in particular along the Topex-Poseidon tracks. However, tests performed in our study have shown that uncertainty values lower than 3 cm lead to unrealistic large-amplitude short-wavelength components in the solution. It is worth noting that the uncertainties published by Hernandez & Schaeffer (2000) with their mean sea surface estimates are formal uncertainties. Our tests suggest that these uncertainties might be slightly underestimated and that a value of 3 cm is likely an averaged uncertainty. A 250-m depth uncertainty was assigned to individual ship
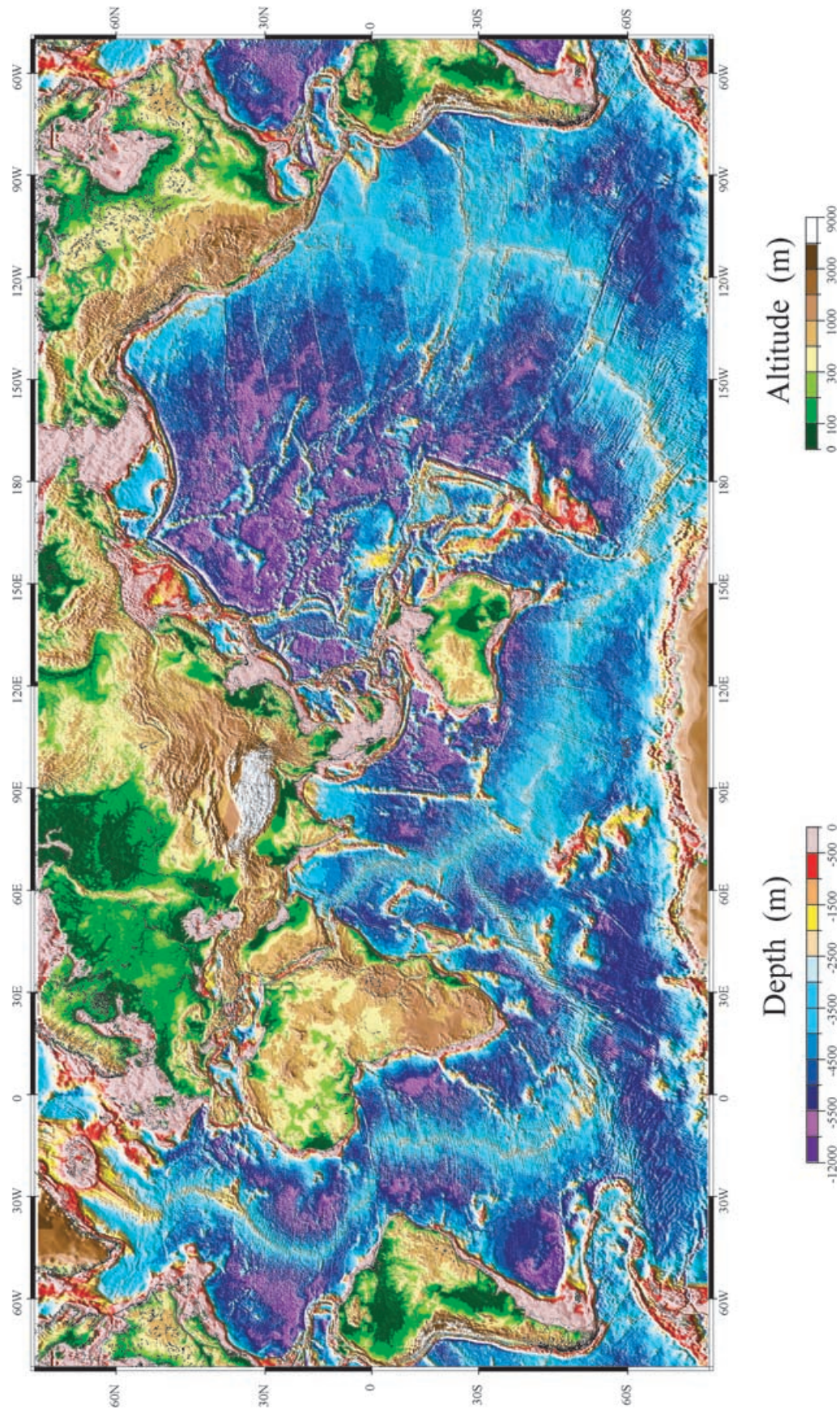
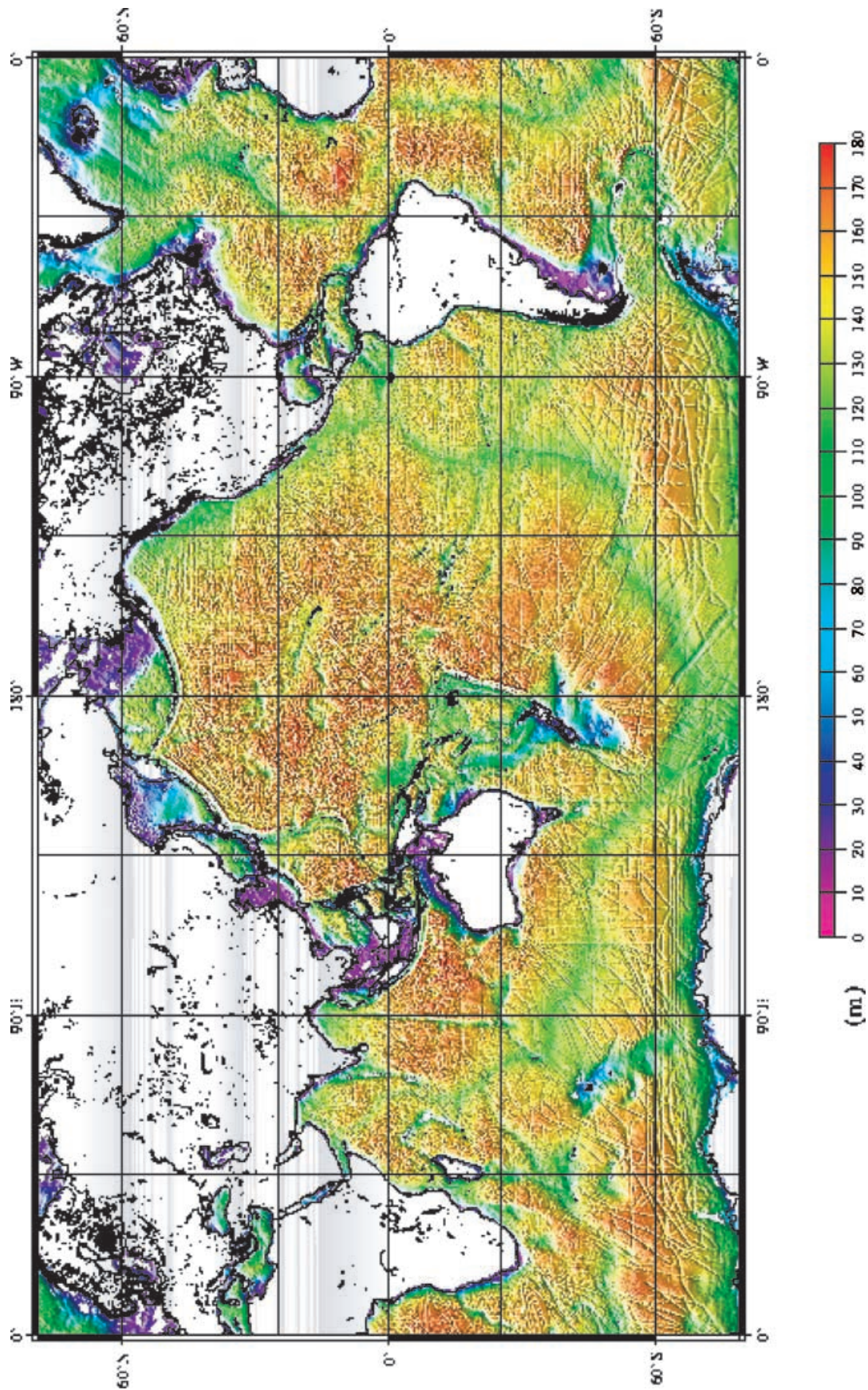**Figure 2.** Worldwide map of the seafloor depths computed in this study (in m).

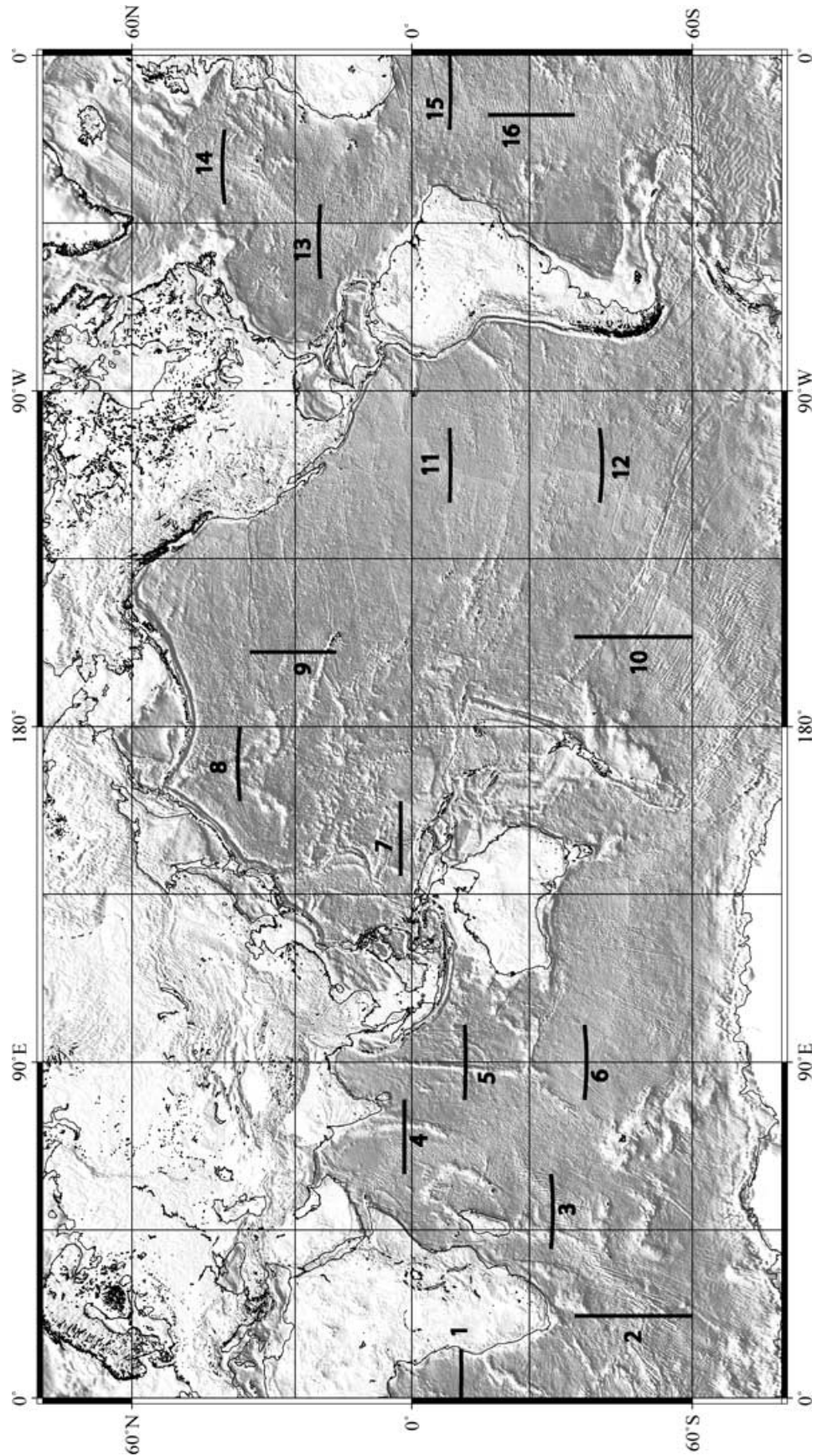**Figure 3.** Map of associated seafloor depth uncertainties (in m).

Figure 4. Location map of the 16 bathymetric profiles presented in Fig. 5.
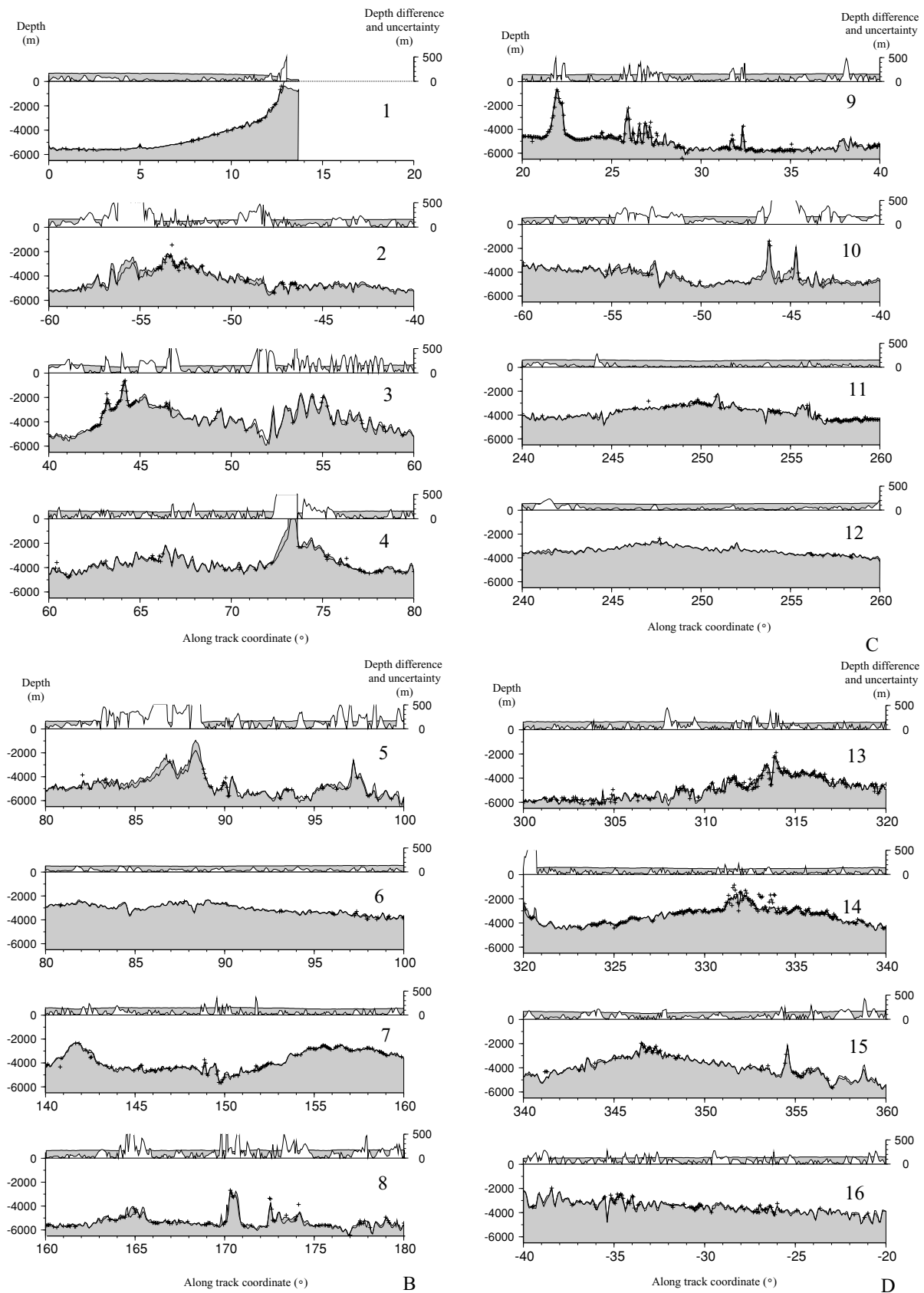
Figure 5. Bathymetric profiles based on three data sources: our solution (grey surface), Smith and Sandwell's solution (solid line) and NGDC data (crosses); referred to left hand abscissa. Upper profiles show the absolute difference between our solution and that of Smith and Sandwell (right hand abscissa) Number associated with each panel refers to the number on the location map (Fig. 4).
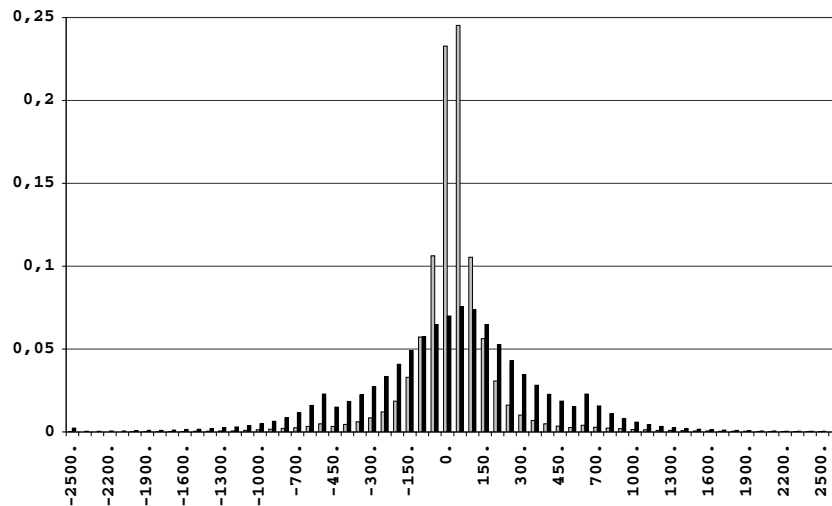
Figure 6. Histograms of depth differences (in m) between our solution and the solutions of Smith and Sandwell (grey bars) and Ramillien and Cazenave (black bars). The vertical axis represents the percentage of data in a given depth range.

sounding data. Tests have shown that this is the lowest admissible value that does not degrade the solution due to erroneous tracks. Note that the relative uncertainties used here for altimetry-derived and shipboard data simultaneously account for both erroneous data and imperfect physical modelling. Table 1 summarizes the numerical values of parameters used in this study.

5 RESULTS

Our global bathymetry solution is based on a two-iteration computational process. Tests performed for a few selected areas have shown that the third iteration departs from the second by at most a few tens of meters. It corresponds to an oscillation between two solutions within the data and model errors. Thus we consider that the solution has mostly converged at the second iteration. Ramillien & Wright (2000) came to a similar conclusion when inverting satellite and *in situ* data in the New Zealand area using the same method.

Smith (1993) checked the quality of ship-sounding data available from oceanographic cruises in major databases. He concluded that the fit of bathymetric maps relative to this data set is not a good indicator of the accuracy of the final map. Because they performed a large amount of work on selection and editing of the echo-sounding data, Smith & Sandwell (1997) developed a procedure that gives a high weight to *in situ* data where available. Similarly, we polished our solution in a two-step procedure. In the first step, we selected a subset of highly reliable *in situ* values from the whole NGDC data set, a subset that we consider as true bathymetric values. Data selection was based on the scatter between all the *in situ* measurements available in the grid cell on the one hand and departure from both ours and Smith & Sandwell's solutions on the other hand. The subset represents about 5 per cent of the whole oceanic domain, and is concentrated at continental margins and around the main islands. In the second step, we corrected our solution for the difference with respect to the actual bathymetry in the subset bins and spline-extrapolated the correction to the surrounding bins. The final solution is presented in Fig. 2.

Fig. 3 is a map of uncertainties computed by combining the *a posteriori* uncertainties and the unit covariance factor χ^2 (eqs 4 and 5). It is worth noting that the solution used in eq. (5) is that output by the inversion scheme, before the polishing procedure, and

that the *in situ* values are the pixel-medians input to the inversion. χ^2 takes a value of 11.4, which means that the formal *a posteriori* uncertainties were globally lower than the mean residuals by a factor $(11.4)^{1/2}$. Formal *a posteriori* uncertainties range from 30 m beneath the sounding tracks to 50–70 m in the deepest basins. Such low values (compared to σ_o) mean that the predicted bathymetry is genuinely constrained by the data set and that it barely reflects the *a priori* solution. Once the *a posteriori* covariance is scaled by the unit covariance factor, the geographical variations of the uncertainties range from ∼100 m to ∼200 m. These values reflect data distribution and errors, as well as the increased uncertainty of the solution with depth. The latter effect is particularly visible on our map where the deep ocean floor exhibits larger uncertainty than features at shallow depth (for instance, mid-ocean ridges, seamount chains). The map also shows that the tighter the constraint on the solution from the data, the smaller the uncertainty. Conversely, the solution mostly reflects the *a priori* value when large uncertainties are derived.

We have compared our bathymetry solution with that of Smith & Sandwell (1997) and that derived from NGDC echo soundings along a set of 16 west–east and north–south profiles evenly distributed in the three main oceans. The location of these profiles is shown in Fig. 4. For the purpose of this comparison, we used the pixel-averaged NGDC data that were constructed for the inversion procedure initially. The map by Smith & Sandwell (1997) is given on a $2' \times 2'$ grid. We have spline-interpolated their map onto our grid mesh. Because Smith & Sandwell's grid has a smaller grid mesh than ours, this interpolation does not degrade its accuracy. Fig. 5 shows, at each of the 16 locations, the NGDC echo soundings (where present) along the tracks, the profiles extracted from our solution, that of Smith & Sandwell (1997), and the absolute difference between these two satellite solutions. The latter profiles show that discrepancies of up to a couple of hundred metres are encountered only at very few places (see, for instance, profiles 2, 5, 7, 8). While many other comparisons could have been made, this small set of comparative profiles suggests that the solutions are quite consistent. However, since the few profiles shown in Fig. 5 have been chosen almost randomly, no generalization can be made.

We also computed the differences between our solution and the solutions by Ramillien & Cazenave (1997) on one hand, and by
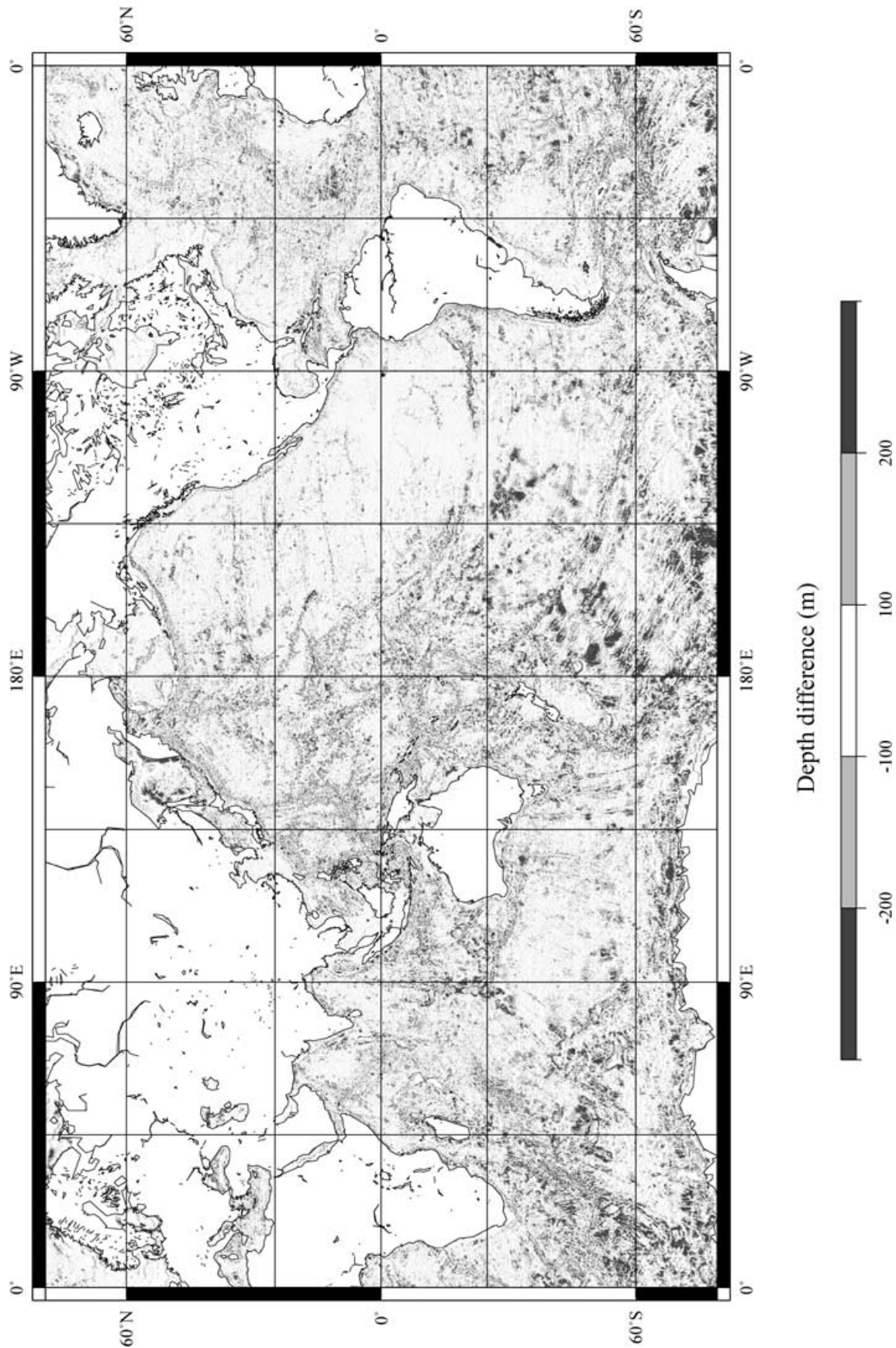
Figure 7. Map of depth differences (in m) between our solution and that of Smith and Sandwell.

Smith & Sandwell (1997) on the other. The standard deviations of the gridded differences (30 million grid points) amount to 650 m and 350 m rms respectively. Fig. 6 shows the histograms of these differences for the two cases. We note that the histogram for the Smih & Sandwell case has a nearly Gaussian shape, with a median value of ∼150 m, an indication that there is almost no systematic bias between the two solutions. On the other hand, the histogram of the differences with respect to the solution of Ramillien & Cazenave is spread towards larger values, while the envelope of the differences is skewed toward positive depth values (our solution is deeper). That our solution fits better the Smith & Sandwell's solution rather than the Ramillien & Cazenave's solution is not surprising. Previous tests performed by Ramillien & Cazenave (1997) have indeed indicated that Ramillien & Cazenave's solution is too smooth (compared to *in situ* bathymetry data) and that it systematically underestimates seamount heights. The shift of the histogram towards positive depth values is less clear. It might reflect the different long-wavelength components (ETOPO-5 in Ramillien & Cazenave and NGDC in the present study), as previously noted by Ramillien & Cazenave (1997) and Smith (1993).

Worldwide differences between our solution and that of Smith & Sandwell are mapped in Fig. 7. The largest differences are found over seamounts, where Smith & Sandwell's solution appears, in general, smoother than ours. Investigating into these differences includes a comparison of the input data used in both analyses: the gravity grid used by Smith & Sandwell (from Sandwell & Smith 1997) and the gravity grid associated with the mean sea surface we used. Such a comparison is indeed possible because Hernandez & Schaeffer (2000) also computed a gravity map together with the mean sea surface. The two gravity grids do not differ by more than ±10 mGal, except in a few limited areas such as the rim of the Antarctic shelf. Most discrepancies occur over rough areas such as seamount chains, where the Sandwell & Smith grid is smoother (see for instance profile 3 in Fig. 5). One or two hundreds of meters of difference in seamount heights can potentially result from such short-wavelength gravity differences, especially in areas devoid of soundings. Smith & Sandwell (1997) used low-pass filters to stabilize the exponential growth of the downward continuation. They also windowed the function used to convert the downward-continued gravity anomalies into bathymetry variations. This may result in a loss of short-wavelength signal and smoothing of rugged relief. Because data uncertainties are analytically accounted for, the inverse method does not excessively damp the short-wavelength signal. This can be observed in Fig. 5, along profile 5, crossing the Ninety East Ridge in the Indian Ocean. The crest of the structure is devoid of echo soundings. Our solution predicts that the ridge is shallower than predicted by Smith and Sandwell.

6 CONCLUSION

The global map of seafloor topography presented in this study has benefited from a map of the mean sea surface that approximates the geoid after transient meteo-oceanographic perturbations were carefully removed. Compared to global bathymetric maps published previously, the original data set and method of derivation are different. This map provides both an alternate solution and an external check for the widely used map by Smith & Sandwell (1997). The two solutions mostly agree within the standard deviations computed in this study, although noticeable differences exist in some areas devoid of soundings. These maps can be used for a variety of scientific applications, over various regions (well charted areas as well as ar-

eas devoid of soundings) and at different spatial scales. It is thus of major importance that investigators be aware of the intrinsic quality of each map from one place to another. Such information is provided here, at least in part, through a map presenting uncertainties. Such a solution can be used to check the shipborn data in the data banks, as evidenced on profile 14 (Fig. 5), where the two altimetry solutions agree with each other but strongly depart from *in situ* data.

Because this study suffered some limitations due to current computational resources, revised versions of that bathymetry map are envisaged. Little improvement is expected to come from the data collected by the ongoing satellite missions. Conversely, better accuracy and finer resolution are foreseen with improved algorithms and bigger computer facilities.

REFERENCES

Baudry, N. & Calmant, S., 1991. 3-D modelling of seamount topography from satellite altimetry, *Geophys. Res. Lett.,* **18,** 1143–1146.

Baudry, N. & Calmant, S., 1996. Seafloor mapping from high-density satellite altimetry, a review, *Mar. geophys. Res.,* **18,** 135–146.

Baudry, N., Diament, M. & Albouy, Y., 1987. Precise location of unsurvyed seamounts in the Austral archipelago area using SEASAT data, *Geophys. J. R. astr. Soc.,* **89,** 869–888.

Calmant, S., 1994. Seamount topography by least-squares inversion of altimetric geoid heights and shipboard profiles of bathymetric and/or gravity anomalies, *Geophys. J. Int.,* **119,** 428–452.

Calmant, S. & Baudry, N., 1996. Modelling bathymetry by inverting satellite altimetry data: a review, *Mar. geophys. Res.,* **18,** 123–134.

Calmant, S. & Cazenave, A., 1987. Anomalous elastic thickness of the oceanic lithosphere in the south-central Pacific, *Nature,* **328,** 236–238.

Calmant, S., Cazenave, A. & Francheteau, J., 1990. Elastic layer thickening with age of the oceanic lithosphere: a tool for prediction of the age of volcanoes or oceanic crust, *Geophys. J. Int.,* **100,** 59–67.

Cazenave, A. & Dominh, K., 1984. Geoid heights over the Louisville Ridge (South Pacific), *J. geophys. Res.,* **89,** 11 171–11 179.

Craigh, C.H. & Sandwell, D.T., 1988. Global distribution of seamounts from SEASAT profiles, *J. geophys. Res.,* **93,** 10 408–10 420.

Dixon, T.H. & Parke, M.E., 1983. Bathymetry estimates in the southern oceans from SEASAT altimetry, *Nature,* **304,** 406–411.

Dixon, T.H., Naraghi, M., McNutt, M.K. & Smith, S.M., 1983. Bathymetric Prediction From SEASAT Altimeter data, *J. geophys. Res.,* **88,** 1563–1571.

Freedman, A.P. & Parsons, B., 1986. Seasat-derived gravity over the musician seamounts, *J. geophys. Res.,* **91,** 8325–8340.

Goodwillie, A.M. & Watts, A.B., 1993. Altimetric and Bathymetric study of elastic thickness in the Central Pacific Ocean, *Earth planet. Sci. Lett.,* **118,** 311–326.

Hernandez, F. & Schaeffer, P., 2000. *Altimetric Mean Sea Surface and Gravity Anomaly Maps Inter Comparisons,* AVISO technical report n AVI-NT-011-5242-CLS, CLS editor, Toulouse.

Jung, W.Y. & Vogt, P. R., 1992. Predicting bathymetry from GEOSAT ERM and shipborn profiles in the South Atlantic Ocean, *Tectonophysics,* **210,** 235–253.

Lambeck, K. & Coleman, R., 1982. A search for seamounts in the Southern Cook Islets, *Geophys. Res. Lett.,* **9,** 389–392.

Lazarewicz, A.R. & Schwank, D.C., 1982. Detection of uncharted seamounts using satellite altimetry, *Geophys. Res. Lett.,* **9,** 385–388.

Mazzega, P. & Houry, S., 1989. An experiment to invert Seasat altimetry for the mediterranean and Black Sea mean surfaces, *Geophys. J. Int.,* **96,** 259–272.

McNutt, M. & Menard, H.W., 1978. Lithospheric flexure and uplifted atolls, *J. geophys. Res.,* **83,** 1206–1212.

Menke, W., 1989. *Geophysical Data Analysis: Discrete Inverse Theory,* Academic Press Inc, Orlando.

Muller, R.D., Roest, W., Royer, J-Y., Gahagan, L. & Sclater, J.G., 1997. A digital map of the ocean floor, *J. geophys. Res.,* **102,** 3211–3214.

National Geophysical Data Center, 1988. ETOPO-5 bathymetry/ topography data, *Data Announc. 88-MGG-02,* Nat. Oceanic and Atmosph. Adm., US Dept. Of Commerce, Boulder.

Nishimura, C.E. & Forsyth, D.W., 1988. Improvement in navigation using seabeam crossing errors, *Mar. geophys. Res.,* **9,** 333–352.

Parker, R.L., 1973. The rapid calculation of potential anomalies, *Geophys. J. R. astr. Soc.,* **31,** 447–455.

Ramillien, G. & Cazenave, A., 1997. Global bathymetry derived from altimeter data of ERS-1 Geodetic Mission, *J. Geodyn.,* **23,** 129–149.

Ramillien, G. & Mazzega, P., 1999. Non-linear altimetric geoid inversion for lithospheric elastic thickness and crustal density, *Geophys. J. Int.,* **138,** 667–678.

Ramillien, G. & Wright, I.C., 2000. Predicted seafloor topography of the New Zealand region: a non-linear, least-squares, inversion of satellite altimetry data, *J. geophys. Res.,* **105,** 16 577–16 590.

Ribe, N.M., 1982. On the interpretation of frequency response functions for oceanic gravity and bathymetry, *Geophys. J. R. astr. Soc.,* **70,** 273–294.

Sailor, R.V., 1982. Determination of the resolution capability of the SEASAT radar altimeter, observations of the geoid spectrum and detection of seamounts, *The Analytical Science Corporation, TR 3751,* Reading, Massachusetts.

Sandwell, D.T., 1984. Thermo-mechanical evolution of oceanic fracture zones, *J. geophys. Res.,* **89,** 11 401–11 413.

Sandwell, D.T. & Smith, W.H., 1997. Marine gravity anomaly from GEOSAT and ERS-1 satellite altimetry, *J. geophys. Res.,* **102,** 10 039–10 054.

Sandwell, D.T. & Smith, W.H., 2000. Bathymetric estimation, in *Satellite Altimetry and Earth Sciences, an Handbook of Methods and Applications,* pp. 44–457, eds Fu, L.L. & Cazenave, A., Academic press, San Diego.

Sharman, 1998. 'GEODAS: A Hydro/Bathy Data management System', *Surveying and Land Information Systems,* Vol. 58, pp. 141–146.

Sichoix, L. & Bonneville, A., 1996. Prediction of bathymetry in French Polynesia constrained by shipboard data, *Geophys. Res. Lett.,* **23,** 2469–2472.

Smith, W.H., 1993. On the accuracy of digital bathymetric data, *J. geophys. Res.,* **98,** 9591–9603.

Smith, W.H. & Sandwell, D.T., 1994. Bathymetric prediction from dense satellite altimetry and sparse shipboard data, *J. geophys. Res.,* **99,** 21 803–21 824.

Smith, W.H. & Sandwell, D.T., 1997. Global seafloor topography from satellite altimetry and ship depth sounding, *Science,* **277,** 1956–1962.

Stein, C.A. & Stein, S., 1992. A model for the global variation in oceanic depth and heat flow with lithospheric age, *Nature,* **359,** 123–129.

Tarantola, A., 1987. *Inverse Problem Theory, Methods for Data Fitting and Model Parameter Estimation,* Elsevier Science Publisher B. V., Amsterdam.

Vogt, P.R. & Jung, W.Y., 1991. Satellite radar altimetry aids seafloor mapping, *EOS Trans. Am. geophys. Un.,* 72, **465,** 468–469.

Watts, A.B., 1978. An analysis of Isostasy in the World's oceans, 1—Hawaii-Emperor seamount chain, *J. geophys. Res.,* **83,** 5985–6004.

Watts, A.B. & Ribe, N.M., 1984. On geoid heights and flexure of the lithosphere at seamounts, *J. geophys. Res.,* **89,** 11 152–11 170.

Watts, A.B., Cochran, J.R. & Selzer, G., 1975. Gravity anomalies and flexure of the lithosphere: a three-dimensional study of the great meteor seamount, Northeast Atlantic, *J. geophys. Res.,* **80,** 1391–1398.

Watts, A.B., Bodine, J.H. & Ribe, N.M., 1980. Observation of flexure and the geological evolution of the Pacific Ocean basin, *Nature,* **283,** 532–537.

White, J.V., Saylor, R.V., Lazarewicz, A.R. & LeSchack, A.R., 1983. Detection of seamount signature in the SEASAT altimeter data using matching filters, *J. geophys. Res.,* **88,** 1541–1551.

APPENDIX

The map is available on the following web site: http://www.omp.obs-mip.fr/omp/gos/bathy/bathy.htm. The $1/16°\times1/16°$ global digital data set can be provided on CDROM on request to the authors.